Journal of Quantitative Spectroscopy & Radiative Transfer 347 (2025) 109652

Contents lists available at ScienceDirect

Journal of Quantitative Spectroscopy and Radiative Transfer

journal homepage: www.elsevier.com/locate/jqsrt

Mid-Infrared line intensity for the fundamental (1–0) vibrational band of carbon monoxide (CO)

D. Michelle Bailey [a,*], Gar-Wing Truong [b,1], Bradley D. Hall [c], Andrew M. Crotwell [c,d], Kimberly J. Harris [a], Jennifer Carney [a], Catherine Nguyen [b], Seth B. Cataño-Lopez [b], Lukas W. Perner [e], Valentin J. Wittwer [e], Thomas Südmeyer [e], Oliver H. Heckl [f], Joseph T. Hodges [a], Garrett D. Cole [b,2], Adam J. Fleisher [a]

[a] Material Measurement Laboratory, National Institute of Standards and Technology, Gaithersburg, MD, USA
[b] Thorlabs Crystalline Solutions, Santa Barbara, CA, USA
[c] Global Monitoring Laboratory, National Oceanic and Atmospheric Administration, Boulder, CO, USA
[d] University of Colorado, CIRES, Boulder, CO, USA
[e] Laboratoire Temps-Fréquence, Institute de Physique, Université de Neuchâtel, Neuchâtel, Switzerland
[f] Optical Metrology Group, Faculty of Physics, University of Vienna, Vienna, Austria

ARTICLE INFO

Keywords:
Cavity ring-down spectroscopy
Carbon monoxide
Line intensity
Mid-infrared

ABSTRACT

Here we apply cavity ring-down spectroscopy to measure the intensity of a rotational-vibrational transition within the fundamental (1–0) vibrational band of carbon monoxide (CO). Laser measurements were made at a wavenumber near 2206 cm^{-1} on a sample of CO-in-air with an amount fraction of $\chi_{CO} = 77.6$ nmol mol^{-1}. High-precision cavity ring-down spectra were acquired using hybrid amorphous-crystalline mirrors to form the optical resonator and by application of simple and robust laser scanning and control techniques. With a relative combined standard uncertainty of $u_S = 0.6$ %, we report the R17 line intensity for the fundamental (1–0) vibrational band of $^{12}C^{16}O$ to be $S = 1.028 \times 10^{-19}$ cm^{-1} $molecule^{-1}$ (isotopologue abundance, $\chi_{iso} = 100$ %; temperature, $T = 296$ K), a value which differs from HITRAN2020 by a relative amount of 2.2 %.

1. Introduction

Reliable spectroscopic reference data are crucial for the accurate evaluation of gas composition by optical diagnostic techniques. Optical spectroscopy methods are often leveraged for applications in trace gas detection, emissions monitoring, and astronomical observation with relevant sensing platforms including ground- [1,2], air- [3,4], and space-borne missions [5–8]. In the case of atmospheric monitoring from space, it is known that variations in spectroscopic reference data can bias results even when the spectroscopy is a minor portion of the overall error budget [9–12]. As a result, many research efforts focus on improving both experimental and theoretical determinations of key line parameters that are used to anchor remote sensing mission observations. In recent investigations, progress in metrology-grade laboratory measurements as well as advances in quantum chemistry theory and calculations have substantially reduced uncertainty in spectroscopic reference data. These high-quality data in turn are expected to improve accuracy in the remote sensing of key molecular species [13–15].

Carbon monoxide (CO) is of keen interest due to its presence as an atmospheric pollutant, a tracer for incomplete combustion processes, and its ability to drive atmospheric chemistry that influences ozone production. Furthermore, the regularity at which CO is detected in various astrophysical objects is growing due to the recent revolution in optical and infrared observatories (e.g., [16]). These applications require self-consistent CO line lists that span broad swaths of the electromagnetic spectrum and comprise transitions involving at least seven quanta of vibrational energy (i.e., up to the (7–0) band) [17]. High-overtone bands in the visible and near-infrared regions have been measured with relative standard uncertainties ranging from 1 % to >10 % [17–20]. One recent study has achieved unprecedented agreement

* Corresponding author.
E-mail address: michelle.bailey@nist.gov (D.M. Bailey).
[1] Present address: Freedom Photonics LLC, Santa Barbara, CA, USA
[2] Present address: Wyant College of Optical Sciences, University of Arizona, Tucson, AZ, USA

https://doi.org/10.1016/j.jqsrt.2025.109652
Received 31 March 2025; Received in revised form 6 August 2025; Accepted 30 August 2025
Available online 31 August 2025
0022-4073/Published by Elsevier Ltd.

(<0.1 %) across laboratories, experimental techniques, and theory for CO line intensities from the second overtone (3–0) band [14,15]. Despite its importance in anchoring any complete line list, no experimental measurements with relative standard uncertainty <1 % are available for the fundamental (1–0) band located in the mid-infrared near a center wavelength of 4.665 μm.

Because rotational-vibrational transitions in the fundamental (1–0) band of CO are strong relative to the overtone bands, it may be unexpected that low-uncertainty measurements of the fundamental band are not already available. However, the application of tunable laser absorption spectroscopy or Fourier transform spectroscopy methods to line intensity measurements of strong bands requires sample cells with short optical pathlengths (mm scale) and low sample pressures (<100 Pa to ≈1 kPa for CO samples with amount fraction $\chi_{CO} > 0.01$ mol mol^{-1}) to achieve acceptable on-resonance transmission (e.g., [19,21]). These restrictions necessitate exceptional length and pressure metrology to deliver low uncertainty measurements of line intensities. Ideally, one would apply state-of-the-art cavity-enhanced spectroscopy techniques (which are based on SI-traceable measurements of time and frequency to determine sample absorption coefficients) to measure line intensities—as is more routinely done in the near-infrared spectral region where telecommunications components are mature (e.g., [14]). However, there are two challenging technical components required to perform cavity-enhanced spectroscopy on strong transitions in this spectral region: 1) high-quality, low-excess-loss cavity mirrors and 2) very low amount fraction CO samples ($\chi_{CO} < 100$ nmol mol^{-1}). Therefore, experiments aiming to leverage the line shape fidelity and SI-traceability of cavity-enhanced methods require new optical instrumentation and precision gas metrology to yield reference-grade spectral data.

Here we employ "hybrid" amorphous-crystalline mirrors with absorption and scattering losses approaching 10^{-6} [22] in a cavity ring-down spectrometer to measure the R17 line intensity in the fundamental (1–0) band of $^{12}C^{16}O$. The sample is from a gas cylinder of CO-in-air with an amount fraction of $\chi_{CO} = 77.6$ nmol mol^{-1}, delivered to the cavity under flowing conditions. Limited by our determination of the CO-in-air amount fraction, we achieve sub-percent relative standard uncertainty in the R17 line intensity and compare with literature values from experiment and theory. The results will serve to anchor efforts in calculating a complete and experimentally accurate CO line list for self-consistent application in atmospheric remote sensing and astrophysical observation—as well as benchmarking quantum chemistry theory for the accurate calculation of spectroscopic properties of small molecules.

2. Description of experiment

2.1. Cavity ring-down spectrometer

Fig. 1 shows the experimental set up. The free-space output of a distributed feedback quantum cascade laser (DFB-QCL) operating at a wavelength near 4.53 μm with >90 mW of optical power was sent through an optical isolator and acousto-optic modulator (AOM) before collection of the AOM first-order output onto a single-mode optical fiber. The optical fiber allowed for a near-Gaussian spatial beam profile to be re-collimated before propagating through a mode-matching lens and coupling into the optical cavity and gas sample cell. The nominally 80 cm long optical cavity with ≈2 cm inner diameter was equipped with low-loss hybrid mirrors [22]. Cavity transmission was monitored by a liquid-nitrogen-cooled indium antimonide (InSb) detector with a cold optical filter to suppress current drifts due to changes in the ambient thermal background. Signal from the photoconductive detector passed through a variable gain transimpedance amplifier (gain setting $G = 10^7$ V/A) and was sent to two digital delay generators (DDG) and a

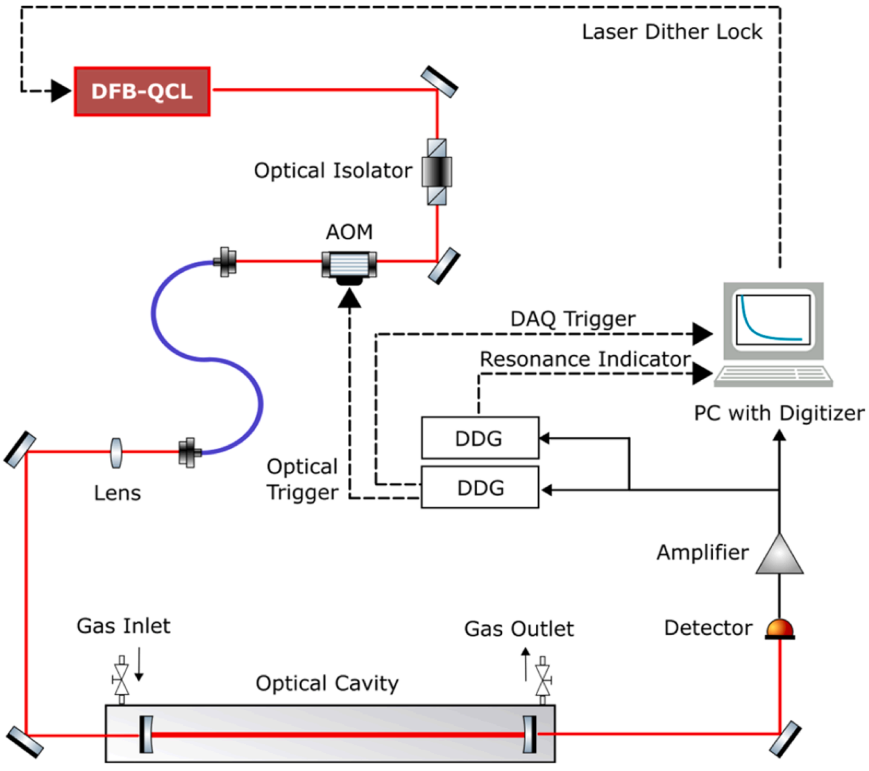

Fig. 1. Schematic of the cavity ring-down spectrometer. The free-space optical output (red lines) from a distributed feedback quantum cascade laser (DFB-QCL) passes through an optical isolator and acousto-optic modulator (AOM) which acts as a fast optical switch before collection into fiber (blue lines) and re-collimation for free-space coupling into the optical cavity. Electronic and instrument control signals are also shown (solid and dashed black lines, respectively). Other abbreviations: DAQ, data acquisition; DDG, digital delay generator; PC, personal computer.

reference-grade, high-speed data acquisition (DAQ) board [23].

The digital delay generators delivered pulsed signals to synchronize 1) laser dither locking of the laser frequency to a cavity resonance and 2) triggering of the AOM to initiate decays and DAQ board acquisition. For laser dither locking to a cavity resonance, a small-amplitude triangle waveform was used to modulate the laser current at a rate of 1 Hz. Laser current dithering parameters allowed for a maximum optical frequency excursion of ±35 MHz to ensure the laser frequency (free-running linewidth of approximately 4 MHz [24]) sampled the nearest cavity resonance during each half-cycle of the triangle waveform. When laser-cavity resonance was achieved and cavity transmission observed, a resonance indicator signal was recorded by the personal computer (PC) and laser dither locking software. Further description of the laser dither locking approach can be found in the literature [25].

To frequency scan the laser, sampling the target CO transition, the laser diode temperature was tuned in increments of approximately 0.03 K, equal to a frequency tuning of one empty-cavity free-spectral-range ($\nu_{FSR,0}$ = 187.28 MHz ± 0.08 MHz). After each $\nu_{FSR,0}$ step, the laser dither locking scheme was again enabled, adjusting the laser current to bring the laser frequency again into resonance with the cavity. Once pre-defined cavity transmission levels (V_{trig} = 0.12 V) were achieved, the laser light was shuttered by the AOM and the metrology-grade DAQ board collected the resulting optical decay signal. When operating under vacuum, an empty cavity decay time (τ) of approximately 117 μs was observed, from which we infer a total per-mirror loss of 22.8×10^{-6} at a wavelength near 4.53 μm. For the measured spectra presented here, 65 decay events were recorded at each cavity resonance in approximately 1 s of laboratory time. Each full scan of the R17 transition, covering >7 GHz detuning range, required about 40 min of laboratory time. The full tuning range of the DFB-QCL is >90 GHz and covers both the R17 and R18 CO transitions; however, due to N_2O present in the gas sample (described in sections 2.2, 2.3, and 3.2.3), the R18 transition could not be included in this study.

2.2. Sample and conditions

In October 2017, the National Institute of Standards and Technology (NIST) gravimetrically prepared a suite of dilute CO-in-air samples by mixing pure CO with a scrubbed natural air balance gas. Those samples—with target CO amount fractions ranging from $\chi_{CO} \approx 30$ nmol mol^{-1} to $\chi_{CO} \approx 180$ nmol mol^{-1}—were characterized for drift relative to a stable internal molecular standard (methane, CH_4; amount fraction ≈1.8 μmol mol^{-1}) using commercial optical analyzers [26] over a more than six-year period (October 2017 to February 2024). From the suite of cylinders, we selected the sample with the smallest apparent drift in CO amount fraction for this study.

The present-day CO-in-air amount fraction of $\chi_{CO} = 77.6$ nmol mol^{-1} ± 0.5 nmol mol^{-1} was assigned on the World Meteorological Organization (WMO) X2014A CO scale by the National Oceanic and Atmospheric Administration (NOAA) Global Monitoring Laboratory [27] using an updated CO drift analysis and correction procedure. The standard uncertainty in χ_{CO} used here is from the updated NOAA analysis and includes uncertainty in 1) the scale realization via drift-corrected primary and secondary standards, 2) the analytical uncertainty in the scale value assignment for our sample, and 3) a post value assignment correction for drift between the time of NOAA analysis and the time of NIST cavity ring-down spectroscopy (CRDS) measurements (≈60 days). Further information regarding the updated drift correction procedure, scale realization, and sample value assignment is available as Supplementary Information.

From within the original suite of NIST gravimetric mixtures, different dilutions of CO-in-air were analyzed by Fourier transform spectroscopy to estimate ^{13}C content (e.g., [28]). From the observed ratio of $^{13}C^{16}O$ and $^{12}C^{16}O$ spectral signatures, the $^{13}C^{16}O$ amount fraction in CO was determined to be 0.0110 mol mol^{-1} ± 0.0003 mol mol^{-1}. Assuming a stochastic distribution of isotopic species, the fractional amount of $^{12}C^{16}O$ in our CO-in-air sample is calculated to be 0.9867 ± 0.0003. The line intensity reported here is corrected to a $^{12}C^{16}O$ fractional amount equal to 1 (i.e., 100 % isotopologue abundance).

For the CRDS measurements, the CO-in-air sample was delivered to the ring-down cavity as a continuous flow and stabilized by a back-pressure controller to values within the range of 2.8 kPa to 10.1 kPa. Sample pressure (p_{cav}) was monitored with an absolute capacitance diaphragm gauge calibrated against a NIST secondary standard and corrected to the center of the cavity by a differential pressure gauge using a model for frictional losses in a flowing system. To monitor sample temperature, *T*, NIST-calibrated platinum resistance thermometers were placed in thermal contact with the front and back portions of the cavity center tube. Temperature readings from the outer wall contact points are assumed to provide the internal gas sample temperature. During laser scanning, sample pressure and temperature measurements were recorded at each frequency step and averaged to provide single mean values for spectral analysis.

We note that the scrubbed natural air balance gas introduced constituent species to the sample chamber. Notably, nitrous oxide (N_2O) was present at >100 ppb amount fraction and required careful treatment in the spectral model. As a known component of the balance gas, the amount fraction was treated as constant across all recorded spectra.

2.3. Spectral analysis

Analysis of the measured absorption spectra was performed using custom spectral fitting codes and cross-checked by the Multi-spectrum Analysis Tool for Spectroscopy (MATS) [29]. Because of residual N_2O found in the scrubbed natural air balance gas, several interfering N_2O transitions near the R17 transition of the CO fundamental (1–0) band were considered in the analysis. A MATS-compatible table of all molecular transitions included in the spectral model is available as Supplementary Data, along with a read me file included as Supplementary Information which describes the MATS-compatible heading structure.

A multispectrum fitting approach was used to extract the line intensity of the R17 transition of the (1–0) band of $^{12}C^{16}O$. Spectra recorded at five different pressures were fitted simultaneously to give a single CO line intensity value. A speed-dependent Voigt profile (SDVP, a limiting case of the Hartmann-Tran profile [30]) was used for the target CO transition and selected N_2O transitions, with initial parameters pulled from the HITRAN2020 spectral database [20]. Fits included a fixed value for the weak line mixing coefficient (Rosenkranz approximation [31,32]) for the target R17 line, estimated from Predoi-Cross et al [33]. During fitting, a frequency axis offset (ν_{offset}) was floated on a per-spectrum basis while the R17 line intensity (*S*), air-broadening coefficient (γ_0), speed-dependent air-broadening coefficient (γ_2/γ_0), sample N_2O amount fraction (χ_{N_2O}), and a relative frequency difference between the R17 line and the interfering N_2O lines ($\nu_{\Delta(CO)}$) were each fitted to single values shared across all measured spectra.

Non-Markovian collisions in CO gas mixtures can lead to observations of apparent intensity depletion when an incomplete line shape is used to fit the transition cores [34]. This bias is greatly reduced for transitions involving higher ground-state rotational levels like the $J'' = 17$ *R*-branch transition studied here. Non-Markovian collisional effects are also smaller at lower pressures. Here, we constrain our investigation of the R17 transition to CO-in-air pressures ≤10.1 kPa. Based on these experimental conditions and on prior observations of the (3–0) band of CO [34], we assume the effect of non-Markovian collisions on our retrieved core line areas to be negligible.

3. Results and discussion

3.1. Fitting results

Fig. 2 shows spectra collected for the R17 transition across five cavity

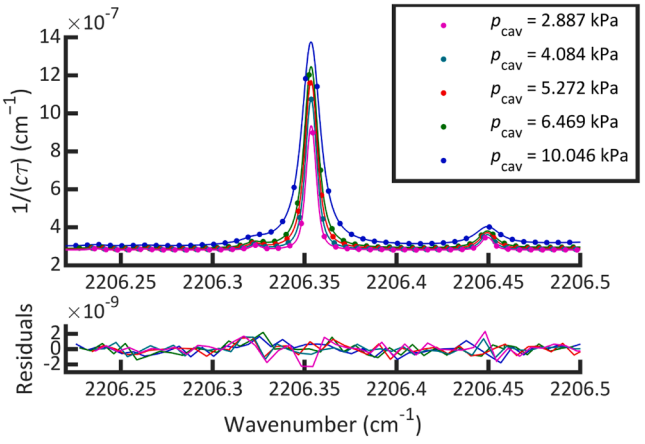

Fig. 2. Multispectrum fit results for the R17 transition of the fundamental (1–0) carbon monoxide (CO) band. The absorption coefficient, $1/(c\tau)$ where c is the speed of light and τ is the cavity decay time constant, is plotted vs. wavenumber in the upper panel. Measured values are plotted as dots, and the fitted model is plotted as lines. The observed-minus-calculated residuals are plotted as lines in the lower panel.

pressures (p_{cav}; dots, upper panel) along with the fitted model (lines, upper panel) and observed-minus-calculated fit residuals (lines, lower panel). For individual spectra, the observed quality factors ranged from 850 to 1610. (Quality factor is defined as the ratio of the maximum CO fitted model absorbance to the standard deviation of the fit residuals.) A list of fit parameter results (excluding the CO line intensity) from an unweighted non-linear least squares fit is shown in Table 1. We note that the fitted air-broadening coefficient is close to the HITRAN2020 value while the speed-dependent coefficient differs by ≈11 % which is slightly larger than the maximum expected combined relative uncertainty (10 %) derived from the HITRAN2020 uncertainty codes.

3.2. Uncertainty budget

3.2.1. Summary

From the multispectrum fit, the R17 line intensity is $S = 1.028 \times 10^{-19}$ cm molecule^{-1}, reported here with a combined standard uncertainty of $\sigma_S = 6 \times 10^{-22}$ cm molecule^{-1}. This quantity is corrected to the HITRAN reference temperature of 296 K and to 100 % relative abundance of the $^{12}C^{16}O$ isotopologue of carbon monoxide. Table 2 shows the relative standard uncertainty components for the experiment. The largest component is from the relative standard uncertainty in the CO amount fraction, $u_{\chi CO} = 0.6$ % (see Section 2.2. *Sample and Conditions*), which dominates the combined relative standard uncertainty of $u_S = 0.6$ %. Other notable contributions include uncertainty associated with the choice of multispectrum fitting method which includes various treatments of the N_2O spectral interference and parameter correlation ($u_{msf} = 0.15$ %) and the pressure ($u_p = 0.13$ %). The remaining contributions noted in Table 2 are attributed to uncertainty in the fit precision, cavity free spectral range (FSR), $^{12}C^{16}O$ relative isotopic abundance (see Section 2.2. *Sample and Conditions*), temperature, optical frequency drift, and choice of line profile.

Table 1
Spectral fit results for the R17 transition of the (1–0) CO band. Fit precision is the standard deviation from the fitting procedure only.

Parameter	Value	Fit Precision	Units
γ_0	0.051 99	0.000 08	cm^{-1} atm^{-1}
γ_2/γ_0	0.089	0.002	
χ_{N_2O}	155.5	1.0	nmol mol^{-1}
ν_{offset} *	0.3	0.2	GHz
$\nu_{\Delta(CO)}$	4.6	0.3	MHz

* Parameter fit on a per spectrum basis and reported here as an averaged result with corresponding standard deviation

Table 2
Uncertainty budget.

Parameter	Value	Relative Standard Uncertainty (u) in S, %	Description
χ_{CO}	77.6 nmol mol^{-1}	0.6	CO-in-air amount fraction
msf		0.15	Multispectrum fitting method
p	2.8 kPa – 10.1 kPa	0.13	Pressure
S_{fit}	-	0.06	Fit precision
ν_{FSR}	187.28 MHz	0.04	Cavity free spectral range
χ_{26}	0.9867	0.03	$^{12}C^{16}O$ relative isotopic abundance
T	297.03 K	0.02	Temperature
$\Delta\nu$		0.02	Optical frequency drift
$g(\tilde{\nu})$	-	0.010	Lineshape function
$u_{c,r}$	-	**0.6**	**Combined**

3.2.2. Pressure correction and leak assessment

For a thorough assessment of the uncertainty in the gas density, it was necessary to correct for the difference between the measured pressure (based on an absolute pressure gauge) and the mean value within the ring-down cavity. To this end, we measured the pressure drop in the system with a differential pressure gauge. We also modeled [35] fully developed internal fluid flow under steady state conditions to verify the observed pressure difference and complete the required correction. Although we found that the pressure drop across the ring-down cavity was negligible, there was an appreciable reduction in pressure between the absolute pressure gauge and the cavity, thus establishing the need for a correction. A summary of the observed sample pressure and temperature conditions is shown in Table 3.

In a flow system like that used here, the frictional losses leading to a downstream reduction in pressure are proportional to the kinetic energy per-unit-volume of the flowing gas, $\rho\overline{V}^2/2$, where ρ is the gas density and $\overline{V}$ is the mean gas velocity in the tube. Here, the properties of air were used as it is the balance gas of the measured sample where the amount fraction of CO is in trace quantities. Assuming laminar internal flow in a tube of internal diameter, *D*, and length, *L*, the pressure reduction is $\Delta p = \frac{64}{Re}\frac{L}{D}\frac{\rho\overline{V}^2}{2}$ in which *Re* is the Reynolds number equal to $4\dot{m}/(\pi D\mu)$, $\dot{m}$ is the mass flow rate and μ is the gas viscosity. Assuming ideal gas behavior, $p = \rho N_A k_B T/M_W$ where *p* is pressure, k_B is the Boltzmann constant, N_A is the Avogadro constant, *T* is the temperature, and M_W is the molecular weight, the change in gas pressure reduces to

$$\Delta p = \left(\frac{128}{\pi}\frac{\mu N_A k T}{M_w}\right)\frac{\dot{m}L}{D^4 p} = F_\mu\frac{\dot{m}L}{D^4 p} \quad (1)$$

where we have used the mass continuity relation, $\dot{m} = \rho\overline{V}A$, to express the mean gas velocity in terms of the mass flow rate and internal cross-sectional area of the tube, $A = \pi(D/2)^2$. For air at a constant temperature $T = 296$ K for which$\mu = 1.846$ x 10^{-5} kg m^{-1} s^{-1} we calculate $F_\mu = 64$ kg m s^{-3}.

Given the potential for variable tubing geometry in the experimental flow manifold, we modeled the differential pressure as the sum of terms described by Eq. (1). We considered three distinct sets of segments denoted as Sections I, II and III corresponding to: I) plumbing from the upstream tee (which links the sample gas to the absolute and differential gauges) to the ring-down cavity inlet, II) the flow path within the ring-down cavity, and III) plumbing from the cavity outlet to the downstream tee, which connects to the other side of the differential gauge and to the cavity exhaust stream.

Sections I and III comprise multiple segments, including flow

Table 3
Observed CO-in-air sample conditions for each spectrum.

Pressure correction, %	Mean cavity pressure, kPa	Combined pressure uncertainty*, %	Cavity temperature difference, K	Mean cavity temperature, K	Combined temperature uncertainty†, %
0.4	2.887	0.13	0.12	297.03	0.019
0.3	4.084	0.07	0.13	297.03	0.02
0.17	5.272	0.05	0.13	297.04	0.019
0.16	6.469	0.04	0.13	297.03	0.02
0.06	10.046	0.04	0.11	297.02	0.018

* Quadrature sum of contributions from the modeled pressure difference for each spectrum, as well as the measured leak rate (0.03 %) and pressure gauge calibration (0.015 %).

† Quadrature sum of contributions from the measured temperature difference and drift, temperature correction to the HITRAN2020 reference value of 296 K [19] (0.012 %) and the temperature probe calibration (0.007 %).

through tees, elbows, valves, rigid and flexible tubing, etc. All components in Section I and III are designed for use with tubing of outer diameter equal to 6.35 mm (0.25 inches) and have manufacturer-specified inner diameters, D, of about 4.57 mm (0.18 inches). The total lengths of Section I and III are $L = 42.7$ cm and $L = 52.7$ cm, respectively. Section II comprises solely the ring-down cell [$D \approx 21.18$ mm, $L = 80$ cm]. Using these values for D and L throughout Sections I, II, and III, and application of Eq. (1), we evaluated the pressure, p, as a function of flow spatial coordinate z. In the top panel of Fig. 3, we illustrate these calculations for the case $p(0) = 2.8$ kPa and a maximum $\dot{m} = 0.8$ mg s^{-1} (40 cm^3 min^{-1}).

From inspection of Eq. (1), we see that $\Delta p/p \propto D^{-4}$ and therefore the relatively large diameter of the sample volume in the ring-down cavity makes the pressure gradient in that region (Section II) negligible by comparison to the gradients within Sections I and III (see the portion of the top panel of Fig. 3 labeled "II"). Moreover, additional estimates of pressure reductions caused by rapid expansion and contraction into and out of the ring-down cavity show that their contributions to the observed pressure gradient also were negligible.

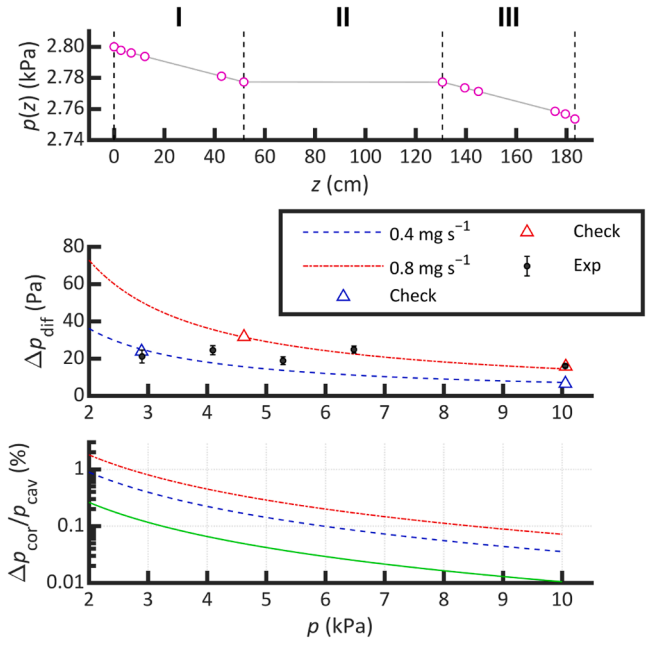

Fig. 3. Top panel. Scaled calculations of pressure, $p(z)$, in Sections I–III vs. flow coordinate, z, based on stepwise application of Eq. (1) for a mass flow rate of 0.8 mg s^{-1} and a gauge reading of $p(0) = 2.8$ kPa. Middle panel. Modeled pressure difference, Δp_{dif}, plotted as a function of $p(0)$ for two bounding flow rate cases (red dot-dashed and blue dashed curves), along with the measured check points (blue and red open triangles) and measured Δp_{dif} values observed during spectral acquisition (black dots). Bottom panel. Relative pressure correction, $\Delta p_{cor}/p_{cav} = p(0)/p_{cav} - 1$where $p_{cav}$is the pressure at the center of the ring-down cavity. The upper two curves correspond to the bounding flow rate cases given in the middle panel. The bottom solid green curve, $u_r(\Delta p_{cor}/p_{cav})$, is the relative standard uncertainty in this pressure correction. This quantity was calculated assuming a uniform probability distribution with a full width at each value of $p(0)$ equal to the difference between the plotted $\Delta p_{cor}/p_{cav}$ values.

We evaluate our flow model by comparison with measurements of the upstream-to-downstream differential pressure at various upstream pressures and flow rates spanning the operating conditions over which the absorption spectra were acquired. The results of this evaluation are shown in the middle panel of Fig. 3. To best match the modeled results (dot-dashed and dashed lines) with several experimental checkpoints (open triangles), we applied a single multiplicative factor of 1.11 ± 0.09 to the model. The multiplicative factor accounts for various assumptions in the model and for uncertainties in values like the volumetric flow rate indicated by the flow meter located downstream of Section III. Overall, the results are in good agreement with the measured differential pressure, exhibiting a linear dependence on mass flow rate and varying inversely with pressure.

Also shown in the middle panel of Fig. 3 are the measured differential pressures for the experimental conditions listed in Table 3. Each spectral acquisition was performed at either one of the two bounding mass flow rates of $\dot{m} = 0.4$ mg s^{-1} or $\dot{m} = 0.8$ mg s^{-1} (20 cm^3 min^{-1} or 40 cm^3 min^{-1}), or at an intermediate mass flow rate of $\dot{m} = 0.6$ mg s^{-1} (30 cm^3 min^{-1}; black dots).

In the bottom panel of Fig. 3 we present the magnitude of this experimentally grounded pressure correction for the two bounding flow rates (dot-dashed and dashed lines), and we give the relative standard uncertainty of this correction. Precise measurements of the upstream-to-downstream pressure difference, bounds on the mass flow rate and the ability to model this profile yield uncertainties in the pressure correction. The relative standard uncertainties in the correction factors ranged from 0.12 % at $p = 2.8$ kPa to 0.01 % at $p = 10$ kPa. Importantly, at our minimum pressure (2.8 kPa) and maximum mass flow rate (0.8 mg s^{-1}), we model that neglect of this pressure correction would increase the sample density by 0.8 %, with the same (negative) relative bias in a single-spectrum measurement of line intensity.

Finally, and in addition to our detailed analysis of pressure difference due to flow, we also tested the cavity for potential leaks while under vacuum and observed a leak rate of 230 μPa s^{-1}. Assuming an amount fraction of $\chi_{CO} = 5$ μmol mol^{-1} in the laboratory air, we estimate the leak contribution to the sample CO amount fraction under flow to be no more than 0.03 %. Finally, calibration of the absolute pressure gauge contributed a relative standard uncertainty of 0.015 %. The quadrature sum of uncertainty components attributed to the maximum differential pressure correction, leak rate, and gauge calibration yields an estimated relative standard uncertainty associated with pressure of $u_p = 0.13$ %.

3.2.3. *Multispectrum fitting method*

To assess the impact of our choices made during the multispectrum fitting process, we repeated the multispectrum fit under various conditions. First, we tested the use of weighting factors in the multispectrum fit. The relative precision in the fitted time constants was observed to

vary across each spectrum, from values of $\sigma_\tau/\tau \approx 0.14$ % in the baseline to $\sigma_\tau/\tau \approx 0.7$ % near peak CO absorption. Using the point-by-point statistical uncertainties to calculate normalized weighting factors, we repeated the multispectrum fit to estimate their influence on the retrieved line intensity.

Next, we tested the influence of the N_2O spectral model using a Monte Carlo analysis. Beginning with the HITRAN2020 uncertainty codes [20], the frequencies and line intensities of nearby N_2O transitions were modified by drawing from normal distributions with standard deviations of 0.001 cm^{-1} and 5 %, respectively. Further, we tested the use of a Voigt profile for all N_2O lines instead of the SDVP (where available). Multispectrum fits were repeated for 100 different random modifications to the N_2O spectrum for several cases.

We note that the N_2O spectrum comprises no less than six different bands, and therefore assessing the uncertainty associated with the N_2O spectral interferences may require a more sophisticated approach. A summary of the N_2O spectrum from experimental fits is shown in Fig. 4. Transitions are labeled using the global quanta identification format $(\nu_1\nu_2l_2\nu_3)$ for the upper and lower vibrational states [36], and the model includes lines from the $^{14}N^{15}N^{16}O$ fundamental band [456, (0001)–(0000)], $^{14}N_2^{17}O$ fundamental band [447, (0001)–(0000)], $^{15}N^{14}N^{16}O$ fundamental band [546, (0001)–(0000)], $^{14}N_2^{16}O$ fundamental band [446, (0001)–(0000)], and two $^{14}N_2^{16}O$ hot bands [446, (0221)–(0220) and (0111)–(0110)].

Tests of the choice of weighting factors and the choice of N_2O spectral model resulted in a scattering of fitted values for the CO line intensity. The root-mean-square deviation of these alternative fits resulted in a relative standard uncertainty from the chosen multispectrum fitting method of $u_{msf} = 0.09$ %.

To test for correlation between the fitted parameters, particularly for correlation between the fitted intensity value and the fitted air-broadening coefficient, we performed a Monte Carlo analysis. In this analysis, we simulated 10,000 spectra of the target CO transition using a speed-dependent Voigt profile at $p = 2.9$ kPa, $T = 296$ K, and a signal-to-noise ratio of 850. Fits of the 10,000 synthetic spectra indicated a standard deviation of S related to correlation between parameters of $u_{cor} = 0.12$ %. Note that this estimate for correlation includes the fitting of spectra at a single pressure and therefore should be considered an upper-bound when estimating the influence of parameter correlation in our constrained multispectrum fitting approach. Conservatively, we add in quadrature u_{msf} and u_{cor} to arrive at the value of $u_{msf} = 0.15$ % reported in the uncertainty budget of Table 2.

3.2.4. Cavity Free Spectral Range

The cavity free spectral range ($\nu_{FSR,0}$) was measured by recording the laser frequency while stabilized to successive modes of the optical cavity. The cavity was pumped to vacuum using a turbomolecular pump, the laser jumped, stabilized, and laser frequency measured by a commercial wavelength meter with a manufacturer-specified accuracy of ±0.2 ppm (≈130 MHz at a wavelength of 4.53 μm). An example data set is shown in the top panel of Fig. 5 (blue dots). A linear fit to the data resulted in the residuals shown in the middle panel (blue dots). An oscillation in the residuals is modeled by a sine wave (red line) and attributed to a stable periodic artifact in the wavelength meter. The fit residuals from a combined linear and sine wave model are shown in the bottom panel of Fig. 5 (blue dots).

Long-term reproducibility in the fitted value of $\nu_{FSR,0}$ for data like that shown in Fig. 5 results in a type-A evaluation of relative standard uncertainty with $u_{FSR} = 0.04$ %, or an average value of $\nu_{FSR,0} = 187.28$ MHz ± 0.08 MHz. Finally, to create the spectral frequency axis, the vacuum value of $\nu_{FSR,0}$ is converted to $\nu_{FSR,air}$ using literature values for the refractive index of air calculated at experimental conditions [37].

Bias in the spectral frequency axis associated with drifts in temperature over the course of a single spectral acquisition was also assessed. Based on the temperature probe measurements, the maximum drift rate observed for the cavity temperature was 0.03 K hr^{-1}. For a cavity system with linear composition of approximately 65 % invar and 35 % stainless steel, this drift rate amounts to an absolute fractional length stability of $|L/(\Delta L)| \approx 3 \times 10^8$, or equivalently an absolute drift in frequency of about 200 kHz at 2206.35 cm^{-1}. Added in quadrature with the type-A evaluation of $\nu_{FSR,0}$ reproducibility propagated out to 45 jumps, the combined estimate of the final cavity mode frequency bias for a spectral acquisition is 3.6 MHz.

These results suggest that the frequency of the final optical cavity mode in any given scan may drift by up to 3.6 MHz relative to its expected value based on the per-jump propagation of a constant cavity free spectral range. Assuming a linear drift rate and letting the 3.6 MHz value be the standard deviation of a normal distribution from which randomly chosen values are drawn, a Monte Carlo analysis of 100 random trials produced scatter in the fitted CO line intensity with a relative standard uncertainty of 0.02 %. Added in quadrature with the precision on the fitted value for ν_{FSR}, the combined relative standard uncertainty in the free spectral range is $u_{FSR} = 0.04$ %.

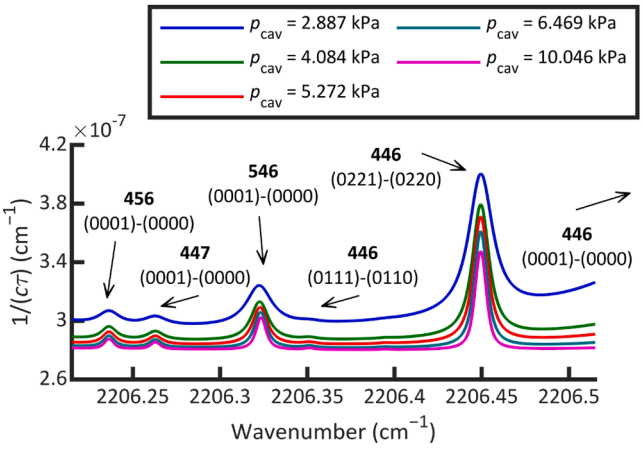

Fig. 4. Fitted nitrous oxide (N_2O) interference spectra. Labels include an isotopocule identifier in bold (e.g., **446** for $^{14}N_2^{16}O$) and a global quanta identifier in the $(\nu_1\nu_2l_2\nu_3)$ format [36].

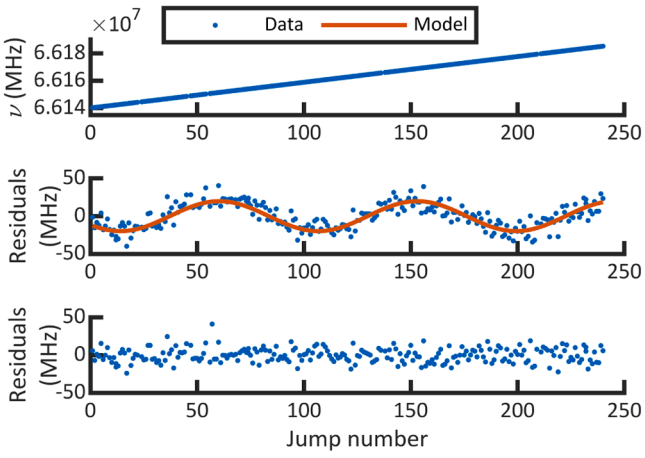

Fig. 5. Laser frequency (ν), measured by the wavelength meter and plotted vs. jump number (top panel, blue dots). At each jump, the laser was coupled to a cavity resonance. A linear fit yielded an estimate of the cavity free-spectral-range ($\nu_{FSR,0}$) and residuals (middle panel, blue dots). A sine wave, fitted to the initial residuals and attributed to a stable periodic artifact in the wavelength meter, is also shown (middle panel, red line). Final residuals from a combined linear-plus-sine-wave model are also shown (bottom panel, blue dots; standard deviation of 9.4 MHz). An average of two measurements performed on different days yielded $\nu_{FSR,0} = 187.28$ MHz ± 0.08 MHz.

3.2.5. Temperature

Temperature was measured by two NIST-calibrated probes in thermal contact with the outside of the optical cavity and sample cell. Temperature readings at each frequency jump were averaged to yield a single temperature value for each spectrum for each probe, and the largest observed difference in the average spectral temperature was 0.13 K. Taking the temperature difference to be the bounds of a uniform distribution, the relative standard uncertainty associated with the temperature gradient is 0.013 %. Added in quadrature with the relative standard uncertainties for temperature probe calibration (0.007 % per probe) and temperature correction to the HITRAN2020 [20] reference temperature of 296 K (0.012 %) yields a combined standard uncertainty for temperature of $u_T = 0.02$ %.

3.2.6. Line profile

The multispectrum fit was performed using a speed-dependent Voigt profile (SDVP) with Rosenkranz line mixing. To test the uncertainty associated with the choice of line profile, we repeated the multispectrum fit with both the Nelkin-Ghatak profile (NGP) and the speed-dependent NGP (SDNGP)—all limiting cases of the Hartmann-Tran profile, HTP [30]. The NGP fit results differed from the SDVP results by a relative amount of −0.3 %, but with significantly reduced quality factors ranging from 440 to 1010 (about 50 % to 60 % worse than the SDVP quality factors). Fitting done with the SDNGP essentially converged to the SDVP, with a relative difference of $u_{g(\tilde{\nu})} = 0.010$ %. The observation of improved quality factors for the SDVP as compared to the NGP is consistent with the observations of Nishiyama et al. in their analysis of Fourier-transform direct frequency comb spectroscopy of CO perturbed by N_2 [38].

3.3. Comparison with the Literature

A comparison between literature values for the R17 line intensity of the $^{12}C^{16}O$ fundamental (1–0) band is shown in Table 4. Each value is expressed relative to HITRAN2020 [20] as the quantity $(S/S_{HT}) - 1$. The cavity ring-down spectroscopy results reported here are in good agreement with the semiempirical line list of Li et al [18], both with values that differ from HITRAN2020 by ≈2 %. The fundamental (1–0) CO band line intensities published in HITRAN2020 [20] are a scaled version of the semiempirical line list of Li et al [18], with a scaling factor of 0.98 chosen based on the Fourier transform spectroscopy (FTS) results of Devi et al [19].

The value reported here is also in good agreement with the *ab initio* quantum-chemistry calculations reported in Zobov et al [39] and Bielska et al [14], which have relative deviations from this work of 0.2 % and −0.4 %, respectively. The experimental value of Zou & Varanasi [21] and the semi-empirically adjusted calculation reported in Balashov et al [17] differ by larger relative deviations of −1.2 %. Larger still is the −1.5 % relative difference with the semi-empirical dipole moment calculations of Meshkov et al [40] and Medvedev & Ushakov [41]. The largest deviation is with the experimental value found in Devi et al [19] which differs from this work by a relative amount of −2.5 %.

Recent measurements of line intensities for the (7–0) overtone band of CO motivated semiempirical adjustments to prior quantum chemistry calculations [14], thus improving agreement between experiment and theory across the (5–0), (6–0), and (7–0) bands [17]. However, from Table V of Balashov et al [17], the semiempirical correction to the calculated line intensities for the (1–0) band show slightly worse agreement with the measured value reported here, relative to the level of agreement with the original calculation [14] shown in Table 4. A further refinement in the *ab initio* methods of Zobov et al [39] appears to improve agreement with our experimental results when compared against Balashov et al [17]. Given these reports, further refinements of the quantum chemistry theory applied to CO are likely required to maintain agreement with experiment for all bands up to at least the (7–0) overtone, especially for the (3–0) band where a high level of agreement between multiple low-uncertainty experiments is observed [14,15].

Table 4
Comparison of measured and calculated R17 line intensities (S) for the fundamental (1–0) band of carbon monoxide ($^{12}C^{16}O$) with HITRAN2020 (S_{HT}) [20].

S,* cm molecule^{-1}	u_S, %	$(S/S_{HT}) - 1$, %	Reference
1.030×10^{-19}		2.4	Zobov et al [39]†
1.028×10^{-19}	0.6	2.2	This work
1.026×10^{-19}		2.0	Li et al [18]
1.024×10^{-19}		1.8	Bielska et al [14]
1.016×10^{-19}	1	1.0	Zou & Varanasi [21]
1.016×10^{-19}		1.0	Balashov et al [17]‡
1.013×10^{-19}		0.7	Meshkov et al [40]; Medvedev & Ushakov [41]
1.006×10^{-19}	2	0	Gordon et al [20]
1.002×10^{-19}	2	−0.4	Devi et al [19]

* Calculated at 100 % isotopologue abundance.
† Estimated from the average shift in "7330 CAS" relative to HITRAN2020 as reported in Table 3 of Zobov et al [39].
‡ Estimated from the average shift in "fit.ai0125" relative to HITRAN2020 as reported in Table V of Balashov et al [17].

4. Conclusion

While the carbon monoxide (CO) amount fraction in high-pressure cylinders of air is known to drift at rates ≈1 nmol mol^{-1} yr^{-1} [26], CO in nitrogen (N_2) is more stable [42]. With our high-precision mid-infrared cavity ring-down spectroscopy system, our measurements of line intensities would benefit from a gravimetric preparation of CO-in-N_2 with minimal N_2O content. Using our reported uncertainty budget and synthetic data modeling for an equivalent ≈80 ppb CO-in-N_2 sample with <1 ppb N_2O and a typically low gravimetric preparation uncertainty of <0.1 % [43], we would expect to measure S with combined relative standard uncertainty ≤0.1 %—towards levels of uncertainty already achieved in the near-infrared for the (3–0) band [14].

Experimental results that achieved this projected level of low uncertainty would provide a critical anchor point for the fundamental (1–0) band to be used in proposed global line list determinations—either through rigorous *ab initio* calculation or through a combined semi-empirical and quantum chemistry approach. The results reported here already indicate that improved semi-empirical corrections to line lists calculated from quantum chemistry first principles [17] are making promising progress as accurate representations of the fundamental (1–0) band of CO. An experimentally accurate, global CO line list would allow comparability and traceability across applications like trace gas sensing, air quality monitoring, and astrophysics and astrochemistry observations.

CRediT authorship contribution statement

D. Michelle Bailey: Writing – review & editing, Writing – original draft, Visualization, Software, Methodology, Investigation, Formal analysis, Data curation. **Gar-Wing Truong:** Writing – review & editing, Validation, Resources, Methodology. **Bradley D. Hall:** Writing – review & editing, Validation, Resources, Methodology. **Andrew M. Crotwell:** Writing – review & editing, Validation, Methodology. **Kimberly J. Harris:** Writing – review & editing, Validation, Resources, Methodology. **Jennifer Carney:** Supervision, Resources. **Catherine Nguyen:** Resources, Methodology. **Seth B. Cataño-Lopez:** Validation, Resources. **Lukas W. Perner:** Writing – review & editing, Resources, Methodology. **Valentin J. Wittwer:** Writing – review & editing, Resources, Methodology. **Thomas Südmeyer:** Supervision. **Oliver H. Heckl:** Writing – review & editing, Supervision, Resources, Methodology. **Joseph T. Hodges:** Writing – review & editing, Project administration, Methodology, Conceptualization. **Garrett D. Cole:** Writing – review & editing,

Supervision, Resources, Methodology. **Adam J. Fleisher:** Writing – review & editing, Writing – original draft, Visualization, Resources, Project administration, Funding acquisition, Formal analysis, Conceptualization.

Declaration of competing interest

The authors declare that they have no known competing financial interests or personal relationships that could have appeared to influence the work reported in this paper.

Acknowledgements

Work by AJF was performed with funding from the CHIPS Metrology Program, part of CHIPS for America, National Institute of Standards and Technology (NIST), U.S. Department of Commerce. DMB, AJF and JTH acknowledge funding from the NIST Greenhouse Gas and Climate Science Program and the National Aeronautics and Space Administration Astrophysics Research and Analysis (NASA APRA) Program. OHH is supported by the Austrian Science Fund (FWF) [DOI: 10.55776/P3604], and financial support by the Austrian Federal Ministry for Digital and Economic Affairs, the National Foundation for Research, Technology and Development and the Christian Doppler Research Association is gratefully acknowledged. Crystalline mirror production was performed in the UCSB Nanofabrication Facility, an open access laboratory. The authors thank Zachary Reed (NIST), Tamae Wong (NIST), and James Whetstone (NIST) for commenting on the manuscript.

Supplementary materials

Supplementary material associated with this article can be found, in the online version, at doi:10.1016/j.jqsrt.2025.109652.

Data availability

Data will be made available on request.

References

[1] Wunch D, Toon G, Blavier J, Washenfelder R, Notholt J, Connor B, Griffith D, Sherlock V, Wennberg PO. The total carbon column observing network. Phil Trans R Soc A 2011;369:2087–112. https://doi.org/10.1098/rsta.2010.0240.
[2] Alden C, Coburn S, Wright R, Baumann E, Cossel K, Perez E, Hoenig E, Prasad K, Coddington I, Rieker G. Single-blind quantification of natural gas leaks from 1 km distance using frequency combs. Env Sci Technol 2019;53:2908–17. https://doi.org/10.1021/acs.est.8b06259.
[3] Johnson M, Tyner D, Szekeres A. Blinded evaluation of airborne methane source detection using Bridger Photonics LiDAR. Remote Sens Env 2021;259:112418. https://doi.org/10.1016/j.rse.2021.112418.
[4] Schwietzke S, Harrison M, Lauderdale T, Branson K, Conley S, George F, Jordan D, Jersey G, Zhang C, Mairs H, et al. Aerially guided leak detection and repair: A pilot field study for evaluating the potential of methane emission detection and cost-effectiveness. J Air Waste Manag Assoc 2019;69:71–88. https://doi.org/10.1080/10962247.2018.1515123.
[5] Suto H, Kataoka F, Kikuchi N, Knuteson R, Butz A, Haun M, Buijs H, Shiomi K, Imai H, Kuze A. Thermal and near-infrared sensor for carbon observation fourier transform spectrometer-2 (TANSO-FTS-2) on the Greenhouse gases observing SATellite-2 (GOSAT-2) during its first year in orbit. Atmos Meas Tech 2021;14:2013–39. https://doi.org/10.5194/amt-14-2013-2021.
[6] Buchwitz M, de Beek R, Burrows J, Bovensmann H, Warneke T, Notholt J, Meirink J, Goede A, Bergamaschi P, Körner S, Heimann M, Schulz A. Atmospheric methane and carbon dioxide from SCIAMACHY satellite data: initial comparison with chemistry and transport models. Atmos Chem Phys 2005;5:941–62. https://doi.org/10.5194/acp-5-941-2005.
[7] Eldering A, O'Dell C, Wennberg P, Crisp D, Gunson M, Viatte C, Avis C, Braverman A, Castano R, Chang A, et al. The Orbiting Carbon Observatory-2: first 18 months of science data products. Atmos Meas Tech 2017;10:549–63. https://doi.org/10.5194/amt-10-549-2017.
[8] Armus L, Megeath S, Corrales L, Marengo M, Kirkpatrick A, Smith J, Meyer M, Gezari S, Kraft R, McCandliss S, et al. Great Observatories: the past and future of panchromatic astrophysics. arXiv:2104.00023 [astro-ph.IM]. https://doi.org/10.48550/arXiv.2104.00023.
[9] Connor B, Boesch H, Toon G, Sen B, Miller C, Crisp D. Orbiting Carbon Observatory: inverse method and prospective error analysis. J Geophys Res Atmos 2008;113:D05305. https://doi.org/10.1029/2006JD008336.
[10] Connor B, Bösch H, McDuffie J, Taylor T, Fu D, Frankenberg C, O'Dell C, Payne V, Gunson M, Pollock R, et al. Quantification of uncertainties in OCO-2 measurements of XCO_2: simulations and linear error analysis. Atmos Meas Tech 2016;9:5227–38. https://doi.org/10.5194/amt-9-5227-2016.
[11] Hobbs J, Drouin B, Oyafuso F, Payne V, Gunson M, McDuffie J, Mlawer E. Spectroscopic uncertainty impacts on OCO-2/3 retrievals of XCO_2. J Quant Spectrosc Radiat Transf 2020;257:107360. https://doi.org/10.1016/j.jqsrt.2020.107360.
[12] Lorente A, Borsdorff T, Butz A, Kasekamp O, aan de Brugh J, Schneider A, Wu L, Hase F, Kivi R, Wunch D, et al. Methane retrieved from TROPOMI: improvement of the data product and validation of the first 2 years of measurements. Atmos Meas Tech 2021;14:665–84. https://doi.org/10.5194/amt-14-665-2021.
[13] Polyansky O, Bielska K, Ghysels M, Lodi L, Zobov N, Hodges J, Tennyson J. High-accuracy CO_2 line intensities determined from theory and experiment. Phys Rev Lett 2015;114:243001. https://doi.org/10.1103/PhysRevLett.114.243001.
[14] Bielska K, Kyuberis A, Reed Z, Li G, Cygan A, Ciuryło R, Adkins E, Lodi L, Zobon N, Ebert V, et al. Subpromille measurements and calculations of CO (3–0) overtone line intensities. Phys Rev Lett 2022;129:043002. https://doi.org/10.1103/PhysRevLett.129.043002.
[15] Hodges J, Bielska K, Birk M, Guo R, Li G, Lim J, Lisak D, Reed Z, Wagner G. International comparison CCQM-P229 pilot study to measure line intensities of selected $^{12}C^{16}O$ transitions. Metrologia 2025;62:08006. https://iopscience.iop.org/article/10.1088/0026-1394/62/1A/08006.
[16] Grant D, Lothringer J, Wakeford H, Alam M, Alderson L, Bean J, Benneke B, Désert J, Daylan T, Flagg L, et al. Detection of carbon monoxide's 4.6 micron fundamental band struture in WASP-39b's atmosphere with JWST NIRSpec G395H. Astrophys J Lett 2023;949:L15. https://iopscience.iop.org/article/10.3847/2041-8213/acd544.
[17] Balashov A, Bielska K, Li G, Kyuberis A, Wójtewicz S, Domysławska J, Ciuryło R, Zobov N, Lisak D, Tennyson J, et al. Measurement and calculation of CO (7–0) overtone line intensities. J Chem Phys 2023;158:234306. https://doi.org/10.1063/5.0152996.
[18] Li G, Gordon I, Rothman L, Tan Y, Hu S, Kassi S, Campargue A, Medvedev E. Rovibrational line lists for nine isotopologues of the Co molecule in the $X^1\Sigma^+$ ground electronic State. Astrophys J Suppl Ser 2015;216:15. https://iopscience.iop.org/article/10.1088/0067-0049/216/1/15.
[19] Devi V, Benner D, Sung K, Crawford T, Li G, Gamache R, Smith M, Gordon I, Mantz A. Positions, intensities and line shape parameters for the 1←0 bands of CO isotopologues. J Quant Spectrosc Radiat Transf 2018;218:203–30. https://doi.org/10.1016/j.jqsrt.2018.06.007.
[20] Gordon I, Rothman L, Hargreaves R, Hashemi R, Karlovets E, Skinner F, Conway E, Hill C, Kochanov R, Tan Y, et al. The HITRAN2020 molecular spectroscopic database. J Quant Spectrosc Radiat Transf 2022;277:107949. https://doi.org/10.1016/j.jqsrt.2021.107949.
[21] Zou Q, Varanasi P. New laboratory data on the spectral line parameters in the 1–0 and 2–0 bands of 12C16O relevant to atmospheric remote sensing. J Quant Spectrosc Radiat Transf 2022;75:63–92. https://doi.org/10.1016/S0022-4073(02)00007-9.
[22] Truong G, Perner L, Bailey D, Winkler G, Cataño-Lopez S, Wittwer V, Südmeyer T, Nguyen C, Follman D, Fleisher A, et al. Mid-infrared supermirrors with finesse exceeding 400 000. Nat Commun 2023;14:7846. https://doi.org/10.1038/s41467-023-43367-z.
[23] Fleisher A, Adkins E, Reed Z, Yi H, Long D, Fleurbaey H, Hodges J. Twenty-five-fold reduction in measurement uncertainty for a molecular line intensity. Phys Rev Lett 2019;123:043001. https://doi.org/10.1103/PhysRevLett.123.043001.
[24] Zhao G, Tian J, Hodges J, Fleisher A. Frequency stabilization of a quantum cascade laser by weak resonant feedback from a Fabry–Perot cavity. Opt Lett 2021;46:3057–60. https://doi.org/10.1364/OL.427083.
[25] Hodges J, Ciuryło R. Automated high-resolution frequency-stabilized cavity ring-down absorption spectrometer. Rev Sci Instrum 2005;76:023112. https://doi.org/10.1063/1.1850633.
[26] Analysis of carbon monoxide in air. GMD Technical Report v2.0, NOAA, https://www.gml.noaa.gov/ccl/docs/TP_analysis_CO_v2.0.pdf; 2019.
[27] Carbon monoxide (CO) WMO scale. https://gml.noaa.gov/ccl/co_scale.html.
[28] Gameson L Report of analysis 839.03-08-038: determination of 13C and 12C concentration in carbon monoxide gas mixtures by fourier transform infrared. 2008.
[29] Adkins E MATS: multi-spectrum Analysis Tool for Spectroscopy. Last revision Jul 19, 2023. https://doi.org/10.18434/M32200.
[30] Tennyson J, Bernath P, Campargue A, Császár A, Daumont L, Gamache R, Hodges J, Lisak D, Naumenko O, Rothman L, et al. Recommended isolated-line profile for representing high-resolution spectrosopic transitions (IUPAC Technical Report). Pure Appl Chem 2014;86:1931–43. https://doi.org/10.1515/pac-2014-0208.
[31] Rosenkranz P. Shape of the 5 mm oxygen band in the atmosphere. IEEE Trans Atennas Propag 1975;23:498–506. https://doi.org/10.1109/TAP.1975.1141119.
[32] Ciuryło R, Pine A Speed-dependent line mixing profiles. J Quant Spectrosc Radiat Transf 2999;67:375–393. https://doi.org/10.1016/S0022-4073(00)00030-3.
[33] Predoi-Cross A, Islam N, Smith M, Devi V, Ivanov S, Buzykin O, Thibault F. Room temperature line parameters of the self- and air-broadened fundamental vibrational transition of carbon monoxide: experimental results and calculations. J Phys Conf Ser 2019;1289:012014. https://iopscience.iop.org/article/10.1088/1742-6596/1289/1/012014.

[34] Reed Z, Tran H, Ngo H, Harmtann J, Hodges J Effect of non-Markovian collisions on measured integrated line shapes of CO.
[35] Fox R, McDonald A. Introduction to Fluid Mechanics. New York: J. Wiley & Sons; 1978.
[36] Rothman L, Jacquemart D, Barbe A, D C, Birk M, Brown L, Carleer M, Chackerian Jr C, Chance K, Coudert L, et al. The *HITRAN* 2004 molecular spectroscopy database. J Quant Spectrosc Radiat Transf 2005;96:139–204. https://doi.org/10.1016/j.jqsrt.2004.10.008.
[37] Mather R. Refractive index of humid air in the infrared: model fits. J Opt Pure Appl Opt 2007;9:470–6. https://doi.org/10.1088/1464-4258/9/5/008.
[38] Nishiyama A, Kowzan G, Charczun D, Ciuryło R, Coluccelli N, Masłowski P. Line-shape study of CO perturbed by N_2 with mid-infrared frequency comb-based fourier-transform spectroscopy. Measurement 2024;227:114273. https://doi.org/10.1016/j.measurement.2024.114273.
[39] Zobov N, Ovsyannikov R, Rogov M, Lebedev E, Tennyson J, Polyansky O. CO line intensities: towards subpercent accuracy of intensities of all bands. J Quant Spectrosc Radiat Transf 2025;345:109510. https://doi.org/10.1016/j.jqsrt.2025.109510.
[40] Meshkov V, Ermilov A, Stolyarov A, Medvedev E, Ushakov V, Gordon I. Semi-empirical dipole moment of carbon monoxide and line lists for all its isotopologues revisited. J Quant Spectrosc Radiat Transf 2022;280:108090. https://doi.org/10.1016/j.jqsrt.2022.108090.
[41] Medvedev E, Ushakov V. Irregular semi-empirical dipole-moment function for carbon monoxide and line lists for all its isotopologues verified for extremely high overtone transitions. J Quant Spectrosc Radiat Transf 2022;288:108255. https://doi.org/10.1016/j.jqsrt.2022.108255.
[42] Lee J, Moon D, Lee J, Lim J, Hall B, Nouvelli P, Brewer P, Miller M, Minarro M, et al. International comparison CCQM-K84 – carbon monoxide in synthetic air at ambient level. Metrologia 2017;54:08016. https://iopscience.iop.org/article/10.1088/0026-1394/54/1A/08016.
[43] Botha A, Janse van Rensburg M, Tshilongo J, Leshabane N, Ntsasa N, Kato K, Matsumoto N, Stummer V, Konopelo L, Kustikov Y, et al. International comparison CCQM-K51: carbon monoxide (CO) in nitrogen (5 μmol mol^{-1}). Metrologia 2010;47:08008. https://iopscience.iop.org/article/10.1088/0026-1394/47/1A/08008.